Article:
Cavazzoni, G., Dall'Ara, E. and Palanca, M. (2025) Microstructure of the human metastatic vertebral body. Frontiers in Endocrinology, 15. ISSN 1664-2392

https://doi.org/10.3389/fendo.2024.1508504

Acta Biomaterialia xxx (xxxx) xxx

Contents lists available at ScienceDirect

Acta Biomaterialia

journal homepage: www.elsevier.com/locate/actbio

Full length article

Degeneration of the nucleus pulposus affects the internal volumetric strains and failure location of adjacent human metastatic vertebral bodies

Giulia Cavazzoni [a], Margherita Pasini [a], Christine L. Le Maitre [b,c], Enrico Dall'Ara [b,c], Marco Palanca [a,*]

[a] Department of Industrial Engineering, Alma Mater Studiorum - University of Bologna, Via Terracini 28, 40131 Bologna, Italy
[b] Division of Clinical Medicine, School of Medicine and Population Health, The University of Sheffield, Barber House, 387 Glossop Road, Sheffield S10 2HQ, UK
[c] Insigneo Institute, The University of Sheffield, The Pam Liversidge Building, Sheffield S1 3JD, UK

ARTICLE INFO

Keywords:
Intervertebral disc degeneration
Spinal metastases
Digital volume correlation
In situ mechanical tests
Failure mode

ABSTRACT

Intervertebral disc (IVD) degeneration is suspected to affect the distribution of stress and strain near the vertebral endplates and in the underlying bone. This scenario is worsened by the presence of metastatic lesions on the vertebrae (primarily thoracic vertebrae (60–80 %)) which increase the risk of fracture. As such, this study aimed to evaluate the effect of IVD degeneration on the internal volumetric strains and failure modes of human metastatic vertebral bodies.

Five human thoracic spinal segments including one vertebra with lytic metastases and one radiologically healthy vertebra (control) were *in situ* tested in pure compression within a μCT scanner (isotropic voxel size = 39μm). Each specimen was tested in the elastic regime before and after inducing mock IVD degeneration (enzymatic degeneration with collagenase); and at failure after IVD degeneration. The volumetric strain field was measured using a global Digital Volume Correlation approach (BoneDVC).

After IVD degeneration, larger maximum (+187 %, $P = 0.002$, 95 % CI= [-4447, -1209]) and minimum (+174 %, $P = 0.002$, 95% CI= [1679, 4258]) principal strains were observed in both metastatic and control vertebrae, with peak differences in correspondence of the IVD anulus fibrosus. IVD degeneration caused a transversal fracture pattern in the vertebrae with failure location onset in the middle portion of the vertebral body and in the cortical shell.

In conclusion, IVD degeneration was found to be a key factor in determining the failure mode, suggesting the clinical relevance of including IVD level of degeneration to assess patients' risk of spinal instability.

Statement of significance: Vertebrae can be affected by pathologies, like bone metastases, while intervertebral discs tend to degenerate during life. Generally, these structures and pathologies are studied separately. In this study, we explored the effects of artificial intervertebral disc degeneration on the mineralised tissues of the vertebrae with metastases. We observed that the induced intervertebral disc degeneration changes the mechanical behaviour of the vertebral trabecular bone. We believe that the findings of this study may influence the scientific community to develop new clinical tools for the prediction of the risk of fracture in vertebrae with spinal metastases, including the degeneration of the intervertebral discs as a parameter.

1. Introduction

A wide prevalence (20–80 %) of oncological patients, especially affected by lung, breast, prostate, kidney and bladder cancers, develop lytic, blastic or mixed bone metastases [1,2]. The spine is one of the most common sites affected by bone metastases (87 % [3]): primarily thoracic vertebrae (60–80 %), followed by lumbar (15–30 %) and cervical vertebrae (<10 %) [4]. In this respect, lytic metastases disrupt the optimized microstructure of the vertebrae focally reducing the bone mineral density [5–7] and may lead to loss of spinal integrity, low back pain, fractures and, in the worst case (i.e. collapse of the upper thoracic vertebrae), to quadriplegia. Pathological fractures may occur in up to 75 % of patients with spinal metastases [8] affecting their mobility and quality of life [9].

* Corresponding author at: Department of Industrial Engineering, Alma Mater Studiorum - University of Bologna, Via Terracini 28, 40131 Bologna, Italy.
E-mail address: marco.palanca@unibo.it (M. Palanca).

https://doi.org/10.1016/j.actbio.2025.01.018
Received 29 August 2024; Received in revised form 24 December 2024; Accepted 9 January 2025
Available online 10 January 2025

We lack reliable tools [10–12] to help clinicians predict the risk of fracture in metastatic patients to manage them with preventive treatments (i.e. vertebroplasty or stabilisation through rods and screws). Indeed, there is a lack of understanding of how the metastatic vertebrae fail and which features of the metastatic spine are associated with the vertebral failure.

Ex vivo and *in silico* studies highlighted the impact of the type, size and position of the metastases on the mechanical properties of the vertebrae, to improve the clinical assessment of the risk of fracture [5, 13–16]. The size of the lytic lesions was found to explain 72 % of the variability in superficial strains experimentally measured with Digital Image Correlation (DIC) [14]. Vertebral-specific finite element models based on high-resolution micro-Computed Tomography (μCT) images were able to explain 76 % of the variability of the compressive failure load of metastatic vertebral body sections [13]. However, these studies used simplified loading conditions, ignoring the distribution of the loads transmitted by the intervertebral discs (IVDs), and did not consider the degeneration level of the IVDs adjacent to the metastatic vertebrae. As regards the loading conditions, *ex vivo* experimental studies showed that different behaviours were observed when vertebrae were loaded with or without IVDs. Whereby loading the vertebrae through acrylic cement pots after the removal of the IVD was associated with a marked and uniform increase of the principal strains [17], lower shear strains [17, 18], higher stiffness and higher ultimate force [18] with respect to loading the vertebrae through the IVDs. Moreover, during the lifetime of an individual, their IVDs may undergo structural changes that lead to their degeneration. Indeed, degeneration starts with changes to the nucleus pulposus (NP), which becomes dehydrated, more fibrotic and less gel-like, and continues by affecting the annulus fibrosus (AF), making it stiffer, weaker with irregular, bifurcated and interdigitated lamellae and interlamellar fissures [19–22]. These structural changes are reflected in different IVD mechanical behaviours and load transfer between the IVD and the vertebral endplate: the compressive load bearing is shifted from the NP toward the AF, creating regions with high stress gradient in the AF [19,23–26]. When loaded through healthy IVDs, the trabecular tissue underneath the centre of the endplates of healthy [27,28] and osteoporotic [29–31] vertebrae experienced higher stresses, as a result of the larger load transferred by the NP. Conversely, degenerated IVDs resulted in a larger load applied to the cortical shell, with a consequent increase of the stress/strain at the periphery (i.e. anterior or posterior regions) [29,30,32].

IVD degeneration may be exacerbated by bone metastases [33,34] in both thoracic and lumbar spine [35], interfering with the diffusion of nutritive from the vertebral body to the adjacent IVD or invading degenerated IVD through a complete or incomplete rupture of the vertebral endplate [33,36–38]. These findings suggest the importance of considering the level of IVD degeneration in the assessment of the mechanical behaviour of the spine and the volumetric strain distribution in the metastatic vertebrae. Indeed, the conjoined degeneration of the bone microstructure and the IVDs may lead to different load sharing between the vertebral body and the IVD, leading to different failure modes and location with respect to healthy spine segment [15,27]. To date, the impact of IVD degeneration on the mechanical behaviour of metastatic vertebrae has not been investigated yet.

This study hypothesises that IVD degeneration affects the internal distribution of strain experienced by the vertebral body with metastatic lesions. As such, this study aimed to evaluate the effect of IVD degeneration on the volumetric strain field and failure location in human metastatic thoracic vertebral bodies tested under axial compression.

2. Materials and method

2.1. Study design

This study was approved by the ethics committee of the University of Bologna (n.113053, 10/05/2021) and of the University of Sheffield (n. 031782, 22/6/2020) and was performed in accordance with the Declaration of Helsinki.

Human metastatic spine segments were prepared from patients with different types of primary tumours. The spine segments were tested in the elastic regime before and after the degeneration of the IVD, combining *in situ* mechanical testing, micro–Computed Tomography (μCT) imaging and Digital Volume Correlation (DVC) analysis. Enzymatic IVD degeneration was induced via needle puncture and injecting collagenase type II in the IVD. Finally, the localization of failure in the vertebral bodies was evaluated.

2.2. Donors and specimen preparation

Three spines from human donors with previous history of spinal metastases, spread from different primary tumours, were obtained through an ethically approved donation programme (Anatomy Gifts Registry, USA). Donors with a history of spinal surgery and spinal fixation, osteoporosis, and fracture signs were excluded. The spines were scanned with a quantitative Computed Tomography (qCT, AquilionOne, Canon Medical Systems Corporation (Toshiba Medical Systems Corporation), Ōtawara, Tochigi, Japan) using a scanning protocol optimized for bone [14] (voltage: 120KVp, current: 200 mA, slice thickness 0.5 mm, in-plane resolution around 0.5 mm) to identify the metastatic vertebral bodies. In addition, for each metastatic vertebra, the size and the location of the metastases were evaluated by manually segmenting the qCT images (Amira2021, ThermoFischer Scientific, USA) [14]. The size of each metastasis was calculated as a percentage of the vertebral body (Table 1).

Five thoracic spinal segments including four vertebrae each were prepared from the three donors (Table 1). Each spine segment consisted of one vertebra with lytic metastases, one adjacent control vertebra without any radiologically relevant sign of metastases from the qCT; and two vertebrae at the extremities. Specimens were prepared by removing all soft tissues (e.g. anterior longitudinal ligaments, periosteum, muscle)

Table 1
Specimens' details.

Spine segment ID	1	2	3	4	5
Donor	A	A	B	B	C
Type of Primary tumour	Lung	Lung	Bladder	Bladder	Breast
Age	79	79	88	88	57
Sex	M	M	M	M	F
Segment	T2-T5	T8-T11	T1-T4	T8-T11	T5-T8
Metastatic vertebra	T3	T9	T3	T10	T6
Type of the metastasis	lytic	lytic	lytic	lytic	lytic
Size of the metastasis (%)	4	5	17	20	19
Anatomical position of the metastasis	Posterior/ Left	Anterior/ Central	Central	Central	Anterior/ Central /Posterior
Enzymatic solution injected (ml)	0.85	0.8	0.82	1.6	0.85
Physiological Load (N)	1265	1238	671	1030	1757
Fracture Load (N)	1951	2050	1079	1917	4044
Apparent Structural Stiffness intact condition (N/mm)	963	796	868	732	1600
Apparent Structural Stiffness degenerated condition (N/mm)	1000	683	716	839	1624

without damaging the IVDs. The posterior elements of each segment were removed using a hand saw in order to fit the specimen into a custom-made radio-transparent loading device [39,40] for mechanical testing inside the μCT. Then specimens were aligned [41] and the two vertebrae at the extremities of the segment were partially embedded in Poly-Methil-Methacrylate (Technovit 4071, Kulzer-technik, Germany). Specimens were kept frozen at −28 °C, thawed for at least 8 h at 4 °C and left at room temperature wrapped in gauzes soaked in Phosphate Buffer Saline (PBS) 1 hour before the test. Each segment was subjected to a maximum of three freezing-thawing cycles to minimise the effect of storage on the mechanical properties of the IVDs [42,43].

2.3. Assessment of intervertebral disc degeneration

In order to assess the initial level of IVDs degeneration, the specimens were scanned with a 1.5T Magnetic Resonance (MR) (Philips Medical System "Ingenia," Germany) using an acquisition protocol optimized for the IVD: Sagittal T2-weighted Turbo Spin Echo (slice thickness = 3.5 mm). All the sequences were acquired without fat saturation. Due to the small size of the specimen, a knee coil was used to fit the specimen inside the MR and each spine segment was immersed in ultrasound gel to increase the signal-to-noise ratio and to mimic the surrounding soft tissues [44,45].

The Pfirrmann Scoring System [46], based on MRI, was assessed for each IVD of the spine segment (Table 2) by a radiologist. Since the Pfirrmann score is mainly developed for lumbar IVDs and could induce a bias when used in thoracic IVDs, the radiographic grading system developed for thoracic IVDs [47] was used to assess the level of the IVDs degeneration. To use Liebsch's grading system, surrogate sagittal X-rays were obtained by projecting the 3D qCT images (slice thickness 0.5 mm, in-plane resolution around 0.5 mm) onto the 2D sagittal plane. The variables "height loss" of each IVD with respect to normalized values [48,49] and the variable "osteophyte formation" were measured on Horos (Horos Project LGPL 3.0; GNU Lesser General Public License, Version 3) following the reported method [47] (Table 2).

2.4. Artificial intervertebral disc degeneration

A validated biochemical model of IVD degeneration was used to degrade the collagen fibres of the NP and reduce the disc height [50–53].

Table 2
Intervertebral disc height and level of degeneration.

Specimen ID	1	2	3	4	5
Cranial IVD	T2/T3	T8/T9	T1/T2	T8/T9	T5/T6
Initial height (mm)	3.18	3.95	3.46	3.65	2.01
Initial Pfirrmann Score (from 1 to 5)	2	4	2	4	2
Initial Liebsch Score (from 0 to 3)	1	1	1	1	1
Central* IVD	T3/T4	T9/T10	T2/T3	T9/T10	T6/T7
Initial height (mm)	3.02	3.50	3.04	4.23	3.78
Initial Pfirrmann Score (from 1 to 5)	2	2	2	2	2
Initial Liebsch Score (from 0 to 3)	1	1	1	1	1
IVD height reduction under load [mm]	0.1	0.1	0.2	0.2	0.2
Caudal IVD	T4/T5	T10/T11	T3/T4	T10/T11	T7/T8
Initial height (mm)	2.90	4.74	2.77	2.89	3.88
Initial Pfirrmann Score (from 1 to 5)	2	2	2	2	2
Initial Liebsch Score (from 0 to 3)	1	1	1	1	1

* The central IVD is the one between the metastatic and control vertebra of each specimen.

Enzymatic digestion of the collagen types I and II [54] was obtained by puncturing (20 G needle) and injecting a solution of Collagenase Type II (Gibco™, 125 U/mg) and PBS with a concentration of 2 mg/ml within the NP of the central IVD of each specimen. Puncturing was performed on the posterior or lateral side (Fig. 1) of the specimens to improve the collagenase solution diffusion, until maximal injection volume was reached, determined by initial solution leakage from the injection site. The amount of injected solution for each IVD is reported in Table 1. Prior to enzymatic IVD degeneration, the specimens, wrapped in gauzed soaked in PBS, were preheated at 37 °C for at least 30 min. After the injection, the specimens were sealed in double plastic bags and left for 2 h in a cell culture incubator at 37 °C.

The height reduction under load (Table 2) of the central IVD after the injection of collagenase was calculated as the minimum distance between the vertebral endplates, before and after degeneration, in physiological loading condition from the μCT images (see paragraph 2.5 for details).

A qualitative assessment of the macroscopic effects of the enzymatic degeneration in the tested specimens was performed by dissecting two (ID2, ID5) out of five specimens in the degenerated disc and adjacent non-degenerated discs after the mechanical tests. The disc with the adjacent vertebra was fixed in 4 % v/v neutral buffered formalin. Following fixation, the specimens were decalcified in 20 % w/v ethylenediaminetetraacetic acid (EDTA) pH 7.4 solution until clear on μCT. Following decalcification, tissues were embedded in paraffin wax and 4 μm sections were prepared and mounted onto positively charged slides. Each slice was stained using Haematoxylin and Eosin (H&E) for tissue morphology, Masson's trichrome for collagen staining, and Alcian Blue/Fast Red for proteoglycans as per standard protocols [55]. Images were captured using an Olympus BX60 microscope and CellSens Entry v1.14 software (Olympus, Southend-on-Sea, UK) and qualitatively evaluated.

2.5. Biomechanical testing

In order to test the different specimens under comparable conditions, a preliminary strain analysis was performed to identify the specimen-specific load. Details of the protocol were widely discussed in [14]. Briefly, an electrodynamic spine simulator (MIB 4.0, Italy) was used to axially compress the specimens (displacement control). 3D Digital Image Correlation (Zeiss Aramis Adjustable, GOM Correlate, Braunschweig, Germany, with four 12 MegaPixels cameras, 75 mm f4.5 lenses) was used to measure the minimum principal strain on the anterior surface of the control vertebra, in real-time, while compressing the specimen. A 50 N preload was initially applied to the specimen, to ensure its stability into the testing machine, followed by ten preconditioning cycles between 0 and 300 N. Each specimen was then loaded with a monotonic compressive ramp (0.05 mm/s) until the minimum principal strains on the anterior portion of the control vertebral body surface reached the magnitude typically associated to physiological activities (i.e. averaged value measured *in vivo* on animals around −2500 με [56–58]). Once the DIC measured that strain target, the associated load was assumed as the "physiological load" (Table 1).

Each spine segment was tested in axial compression within a manually operated jig able to fit into the μCT scanner. The jig was equipped with a 10 kN load cell (1-C9C/10 kN, HBM, Germany) and a 20 mm Linear Variable Displacement Transducer (WA20, HBM, Germany). Signals were acquired using an external amplifier and acquisition system (Spider6, HBM, Germany). Each specimen was kept wrapped in gauzes soaked in PBS during the entire test. The cranial pot was fully constrained in the jig while the caudal pot was allowed to axially move to compress the specimen. Any possible bending or torsional movements were related to the compliance of the segment including three IVDs. The loading protocol consisted of i) preloading (50 N) the specimen (load ramp at 0.05 mm/s), ii) preconditioning and loading (load ramp) the specimen before degeneration until the physiological load in 10 s; iii) preconditioning and loading (load ramp) again the specimen after

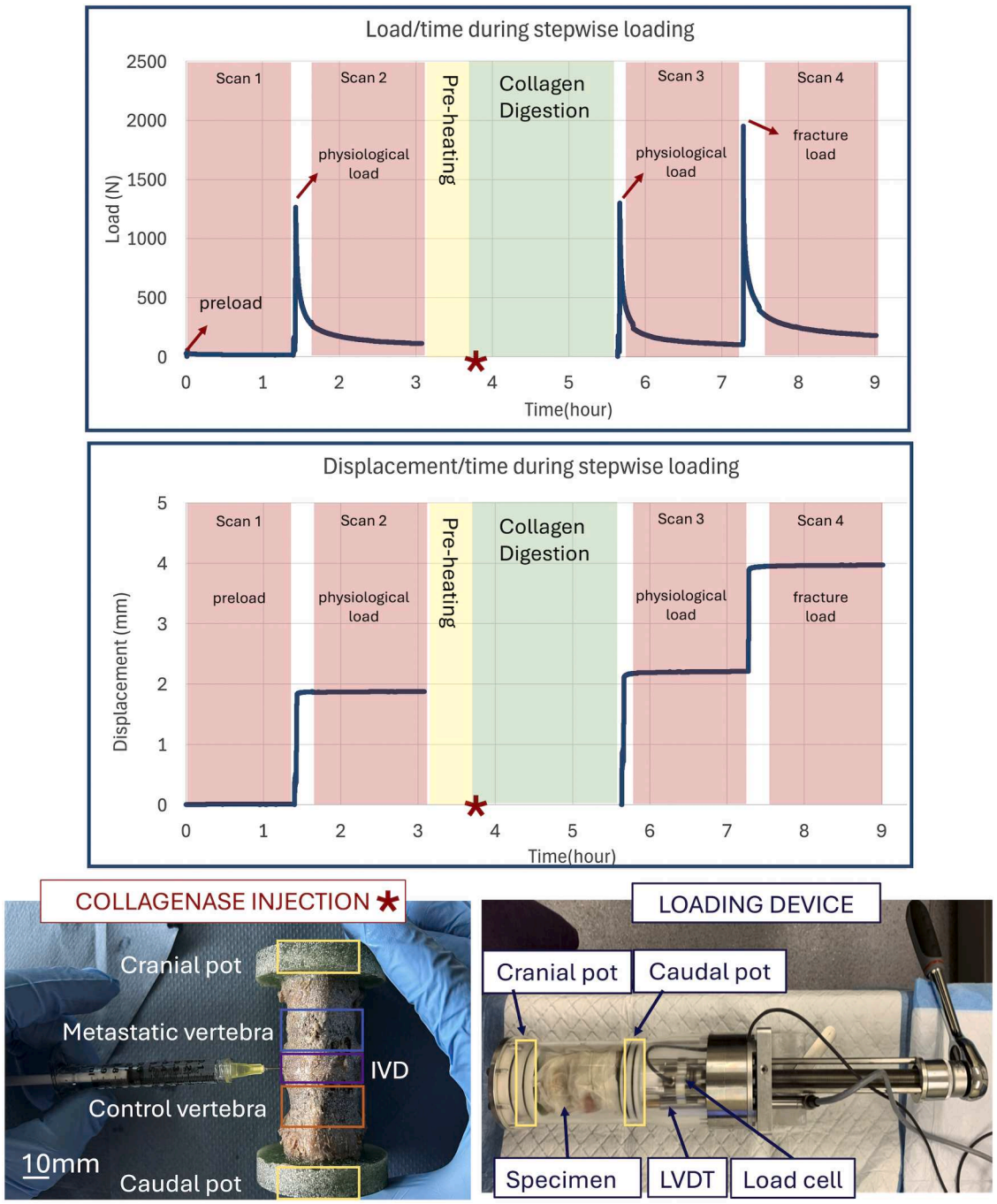

Fig. 1. Example of the load/time and displacement/time curves acquired during a time-lapsed test of a spine segment. The definition of the physiological load for each specimen was reported in [14]. The injection of collagenase within the central intervertebral disc (IVD) of the specimen is displayed on the bottom left. The custom jig for *in situ* mechanical tests is displayed on the bottom right.

degeneration until the physiological load (the same load reached before degeneration) in 10 s; iv) loading (load ramp at approximately 0.1 mm/s) the specimen until failure, which was identified as the first abrupt drop of the axial load (Table 1). After the application of each of these load steps, the loading plate was left in the corresponding position (preload, physiological load, or failure load) for 15 min to allow specimen relaxation (around 85 % of the initial force was lost after 15 min of relaxation), and the specimens were μCT scanned (VivaCT80, Scanco, Switzerland) [15].

Specimens were scanned in preloaded condition (Scan1), in physiological loading condition before degeneration (Scan2), in physiological loading condition after degeneration (Scan3) and at failure (Scan 4) (Fig. 1). Scans were performed using an acquisition protocol optimized for vertebral bodies [15,16,40] (i.e. current 114 mA, voltage 70 kVp, integration time 300 ms, power 8 W, 750 projection/180°, isotropic voxel size 39 μm). Reconstruction was performed using the software provided by the manufacturer, which included a polynomial beam hardening correction equation obtained with a 1200 mg HA/cm^3 density phantom [59].

A global DVC algorithm, BoneDVC [60], was used to measure the full-field displacement and strain distribution in metastatic and control vertebrae, in elastic regime (before and after degeneration) and at failure. The DVC operating principles [61–63] and its measurement uncertainty [64] are largely reported in the literature, also for similar

specimens [6].

Before the application of the DVC algorithm, the images were pre-processed as previously reported [6]. A binary volume-of-interest mask (background equal to 0 and bone equal to 1) was created for the application of the DVC only in the vertebral bodies. A measurement spatial resolution of 100 voxels (3.90 mm) was used for the measurement of the strain field in the elastic regime (Standard Deviation of the Error equal to 291 με [6,65]). A measurement spatial resolution of 50 voxels (1.95 mm) was used for the measurement of the strain field at failure (Standard Deviation of the Error equal to 530 με) [6].

2.6. Assessment of the mechanical behaviour of the vertebral bodies

The maximum principal strains (Eps1) and the minimum principal strains (Eps3), within the vertebral bodies, were measured before (later referred to as "intact condition") and after (later referred to as "degenerated condition") IVD degeneration, in physiological loading condition. Strains in intact condition and degenerated condition were compared to evaluate the changes in the mechanical behaviour of the vertebrae.

In order to evaluate the local effects of IVD degeneration, each vertebra was divided into 27 subregions of interest (subROIs) (Fig. 2), using a custom-made MATLAB (MathWorks, USA) script [40,66]. First, the vertebral body was equally divided into three axial regions of interest (ROIs) according to the distance from the central IVD: far, middle, and close. Subsequentially, to characterize the different sub-regions of the vertebral body, the cross-section of each ROI was divided into nine subregions of interest (subROIs): anterior left (AL), anterior (A), anterior right (AR), left (L), central (C), right (R), posterior left (PL), posterior (P), posterior right (PR). Principal strains were computed for each subROI. To avoid local peak strains, subROIs including <8 DVC nodes were excluded [60].

The Percentage Median Strain Difference (PMSD) [14] due to the degeneration of the IVD was evaluated as the difference between the median strain measured in intact condition and degenerated condition, divided by the median strain calculated in the same region in intact condition. The PMSD was calculated for the entire metastatic and control vertebral bodies, and in the different subROIs of the vertebra.

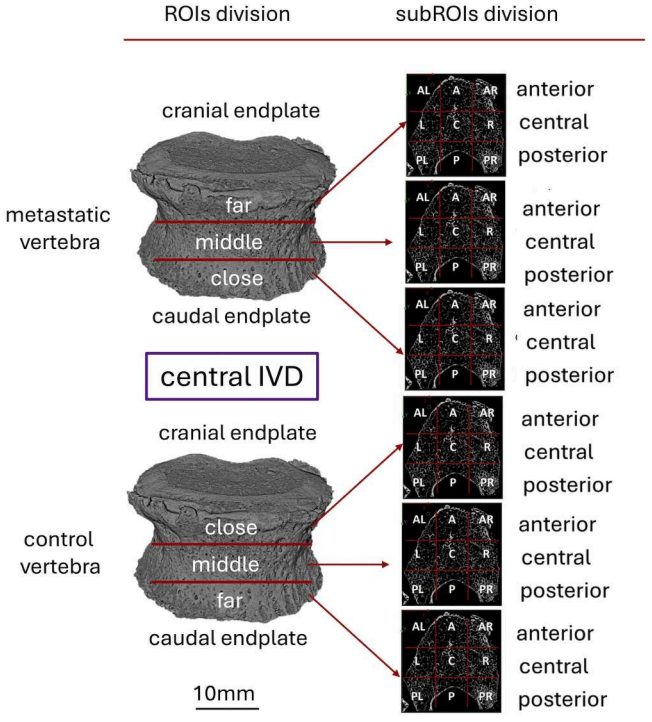

Fig. 2. Left: Division of the vertebra in three ROIs close, middle and far from the central disc of each segment. Right: Division of each ROIs in nine subROIs in the anterior (AL, A, AR), central (L, C, R) and posterior (PL, P, PR) portion of the vertebral body.

Eps1 and Eps3 were measured at failure and 3D colour maps of Eps3 were analysed to identify the location of the failed tissue. In order to visualise the failure location in three dimensions (3D), "Scan4" was aligned and rigidly registered to "Scan1" (Amira2021, ThermoFischer Scientific, USA, alignment of principal axis and Lanczos interpolation). Then the images were processed as reported in [15]: they were binarized using the Max Entropy thresholding algorithm on ImageJ and overlapped using different colours (red: unloaded scan, green: failure scan, yellow: overlapped) to highlight the failure location in metastatic or control vertebrae. The 3D colour maps of Eps1 and Eps3 and the overlapped μCT scans were reported in the Supplementary Materials for each specimen to visualise the portions of the vertebrae with the larger strains and identify the failed region.

2.7. Statistical analysis

Normality of the data distribution (for the entire vertebra and for each subROI) was tested through the Shapiro-Wilk test. If data met the normal distribution, homoscedasticity was tested through Levine's test. Median, and interquartile range (IQR, exclusive median) were reported for all data.

Differences in the maximum and minimum principal strains between the intact and degenerated conditions, in the elastic regime, were evaluated:

- in the metastatic and control vertebrae (pooled data) using the Wilcoxon test, since the data did not meet normal distribution.
- in the metastatic vertebrae using the paired *t*-test, since the data met normal distribution.
- in the control vertebrae using the paired *t*-test, since the data met normal distribution.
- in the subROIs of the metastatic and control vertebrae (pooled data), using paired *t*-test when the data met normal distribution and Wilcoxon test when the data did not meet normal distribution.

For the physiological loading condition, differences in the maximum and minimum principal strains between the metastatic and control vertebrae in intact and degenerated conditions, separately, were evaluated using the Student *t*-test for normal and homoscedastic data; and the Student *t*-test with Welch correction for normal and heteroscedastic data.

At failure, differences in the maximum and minimum principal strains between the metastatic and control vertebrae were evaluated using Student *t*-tests, since data were normal and homoscedastic.

All statistical analyses were performed in Jamovi (Version 2.3, The Jamovi Project 2023) [67] with a significance level set at 0.05 and 95 % confidence interval (95 % CI).

3. Results

3.1. Validation of the artificial intervertebral disc degeneration

The macroscopic visual investigation showed the key features of demarcation and fissures, and the absence of the gelatinous NP in comparison with the adjacent not degenerated IVDs (Fig. 3 A, E). Histological examination demonstrated the presence of cracks and fissures within the NP of collagenase injected (Fig. 3F) with respect to non-injected (Fig. 3B). Lower staining intensity was found for both Masson's trichrome (Fig. 3G) and Alcian Blue (Fig. 3H) within the degenerated NP with respect to the non-injected NP (Fig. 3C, D), which also showed regions of low collagen staining, most likely due to some degree of baseline degeneration. The cartilaginous endplates (CEP) retained collagen staining even in collagenase injected IVD, demonstrating

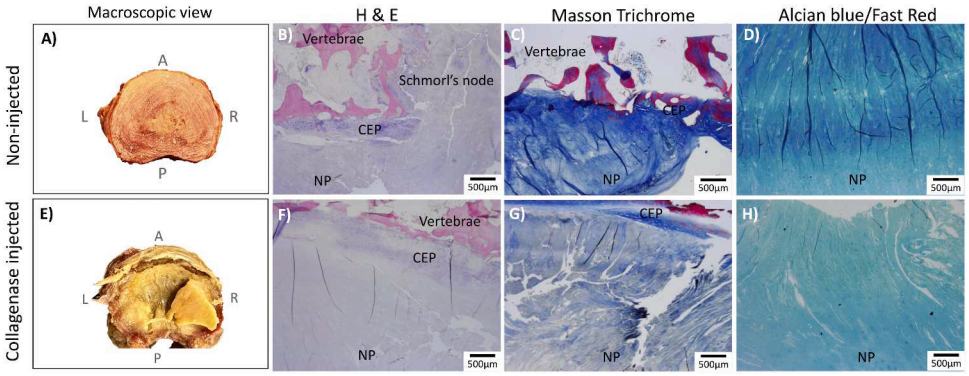

Fig. 3. Macroscopic images of Non-injected (A) and Collagenase injected (B) IVDs. Histological staining of non-injected (top line) and collagenase (bottom line) digested IVDs, staining shown with H&E demonstrating overall morphology (B, F), Masson trichrome shows collagens in blue and other tissue components in red (C, G), and Alcian blue/Fast Red stains proteoglycans blue (D, H). A decrease in collagen staining intensity was observed in collagenase injected discs (G) compared to non-injected discs (C). This was associated with a small decrease in Alcian blue staining intensity (D, H). Regions labelled: Vertebrae, Cartilaginous Endplate: CEP, Nucleus pulpous: NP along with a visible region of Schmorl's node within one disc. Scale bars = 500µm.

restraint of collagenase effects within the NP region (Fig. 3F-H).

3.2. *Mechanical behaviour in the elastic regime for healthy and metastatic vertebrae*

The maximum principal strains (Eps1) within each specimen before and after degeneration were not normally distributed. Eps1 after IVD degeneration were significantly larger (when the data of metastatic and control vertebrae were pooled, +187 % (IQR 99 to 220 %) than in the intact condition ($P = 0.002$, 95 % CI = [−4447, −1209]) (Fig. 4). The metastatic vertebrae experienced 1111 με (IQR 737 to 2084 με) and 4289 με (IQR 2072 to 6764 με), before and after IVD degeneration. The PMSD_Eps1 ranged 30 %−947 %. The control vertebrae experienced 1297 με (IQR 585 to 1326 με) and 3553 με (IQR 1407 to 4273 με) before and after IVD degeneration, with a PMSD_Eps1 between 109 % and 254 %. The Eps1 in the same controls were different before and after degeneration ($P = 0.017$, 95 % CI= [−3348, −570]) (Fig. 4). No significant differences were found between metastatic and control vertebrae in intact condition and in degenerated condition ($P > 0.371$). See Supplementary Materials for details about each specimen (Fig. S1).

The minimum principal strains (Eps3) within each specimen before and after degeneration were not normally distributed. Eps3 after IVD degeneration were significantly larger (when the data of metastatic and control vertebrae were pooled, +174 % (IQR 96 to 230 %)) than in the intact condition ($P = 0.002$, 95 % CI= [1679, 4258]) (Fig. 4). The metastatic vertebrae experienced −1395 με (IQR −1095 to −2415 με) and −5002 με (IQR −3071 to −7027 με), before and after IVD degeneration. The PMSD_Eps3 ranged 42 %−640 %. The control vertebrae experienced −1365 με (IQR −1250 to 1459 με) and −3857 με, (IQR −2917 to 4223 με) before and after IVD degeneration, with a PMSD_Eps3 between 78 % and 202 %. Paired *t*-test revealed that median Eps3 before and after IVD degeneration were different for both metastatic ($P = 0.044$, 95 % CI= [143, 6570]) and control ($P = 0.003$, 95 % CI= [890, 2984]) vertebrae (Fig. 4). No significant differences were found between metastatic and control vertebrae in intact condition and in degenerated condition ($P > 0.188$).

3.3. *Mechanical behaviour in elastic regime in the subregions of interest*

The number of DVC nodes included in each subROI varied from 14 to 60. The maximum (Eps1) and minimum (Eps3) principal strains before and after degeneration were not normally distributed within the

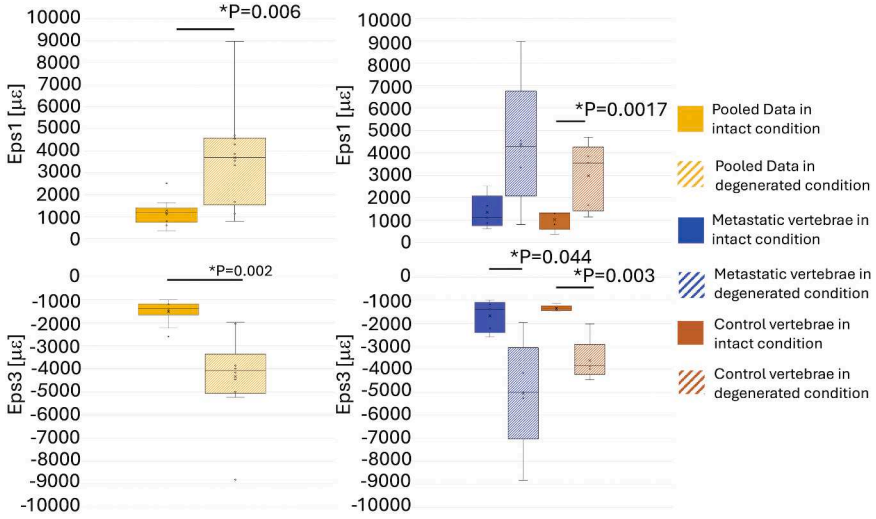

Fig. 4. Boxplot of the Eps1 (top) and Eps3 (bottom) in vertebrae, loaded in physiological load, in intact and degenerated conditions reported in solid and stripes colour, respectively. In yellow, pooled data for metastatic and control vertebrae; in blue, data from metastatic vertebrae; in orange, data from control vertebrae. The boxes are limited by the first and the third quartile. Whiskers represent the lowest and highest data point in the data set excluding any outliers. Mean and median values over the group are represented by a cross and a horizontal line, respectively. Statistically significant differences between intact and degenerated conditions are highlighted with *.

subROIs of metastatic and control vertebrae. The Eps1 and Eps3 measured in each subROI were significantly larger after IVD degeneration for metastatic and control vertebrae (pooled data) ($P < 0.05$) except for the anterior left subROI close ($P = 0.057$) and far ($P = 0.133$) from the degenerated IVD.

Eps1 increased substantially in the left (L) (+196 %, CI = [97, 243]), PL (median +193 %, CI = [114, 294]), and the P (+193 %, CI = [111, 289]) subROIs, and increased moderately in the anterior right (AR) (+117 %, CI = [70, 180]), R (+122 %, CI = [88, 210]) and C (+148 %, CI = [123, 208]) regions.

Eps3 increased substantially in the PL (median +226 %, CI = [135, 297]), PR (+190 %, CI = [111, 256]), and L (150 %, CI = [124, 205]) subROIs, and increased moderately in the central (C) (+112 %, CI = [76, 133]), AR (+118 %, CI = [67, 179]) and A (+128 %, CI=[105, 154]) subROIs.

Despite the lower magnitude of Eps1 and Eps3 with respect to the metastatic vertebrae, the control vertebrae experienced the largest increments of Eps1 and Eps3 after degeneration in the lateral (ranged between +102 % and +232 %, +83 % and +289 %, respectively) and posterior (ranged between +122 % and +358 %, +89 % and +321 %, respectively) subROIs (Fig. 5).

3.4. Mechanical behaviour at failure

At failure, the Eps1 (median on the vertebral body) ranged from 1739 με to 12871 με (IQR 3527 to 11903 με) and from 2098 με to 12234 με (IQR 2854 to 10742 με) in the metastatic and control vertebrae, respectively. Median Eps3 ranged from −15876 με to −2614 με (IQR −4197 to −13219 με) and from −13798 με to −2429 με (IQR −3233 to −13070 με) in metastatic and control vertebrae, respectively. No significant difference was found between metastatic and control vertebrae for the median Eps1 ($P = 0.68$, 95 % CI = [−5078, 7391]) and Eps3 ($P = 0.871$, 95 % CI = [−8015, 6926]).

3D strain colour maps showed those regions of the metastatic and control vertebrae with strains beyond the bone failure strain (approximately −10000 με) (Fig. 6). Eps1 strain peaks and regions with strain concentrations were observed and measured in each metastatic vertebra. Eps3 strain peaks were observed and measured in all the metastatic vertebrae except for specimen ID3 which exhibited strain concentrations of larger magnitude in the control vertebra (see Supplementary Materials for details about each specimen, Fig. S2). In four out of five specimens (ID2, ID3, ID4 and ID5) the failure occurred in the mid-height of the metastatic and/or control vertebral body, leading to a shift of the endplate (Fig. 6, see Supplementary Materials for details about each specimen, Fig. S3, S4, S5, S6). In particular, specimens ID3 and ID4 exhibited strains above the bone failure strain (−10000 με) [68] in both the metastatic and control vertebra and localised the failure in the anterior portion of the cortical shell and in the trabeculae at the mid-height of the vertebral body (Fig. 6). In addition, in specimen ID3 strain concentrations were also observed in the cranial vertebral endplate, close to a non-degenerated IVD. Conversely, in specimen ID1 the onset failure was in the superior endplate of the metastatic vertebra, close to a non-degenerated IVD with a strain pattern similar to that reported in [15].

4. Discussion

This study aimed to experimentally explore the consequences of intervertebral disc degeneration on the local volumetric strain in adjacent radiologically healthy and metastatic vertebrae. To achieve this aim, spine segments in intact condition were mechanically tested *in situ* in the elastic regime. Artificial degeneration was induced through collagenase type II, which targets both collagen types I and II [54]. This degeneration was relatively quick (2 h) and avoided the degradation of the adjacent bone structures [69] and of the other IVDs (Fig. 3). Then, the spine segments were tested again in the elastic regime and up to failure. This approach allowed us to compare the deformation field in intact and degenerated conditions in the elastic regime, and to evaluate, for the first time, the failure location for healthy vertebrae and vertebrae with metastatic lesions adjacent to degenerated IVDs.

In this study, to confirm the effects of the enzymatic degeneration, two out of five specimens were characterised using histological staining (Fig. 3) for the identification of the key features of demarcation and fissures, and decreased collagen within the NP, typical of a degenerated disc [21,22].

The main results of the mechanical tests demonstrated that IVD degeneration significantly affected the mechanical behaviour of the adjacent vertebrae in the elastic regime, increasing the mechanical strains in both metastatic and control vertebrae. The utilised sample showed no significant differences between the averaged strains

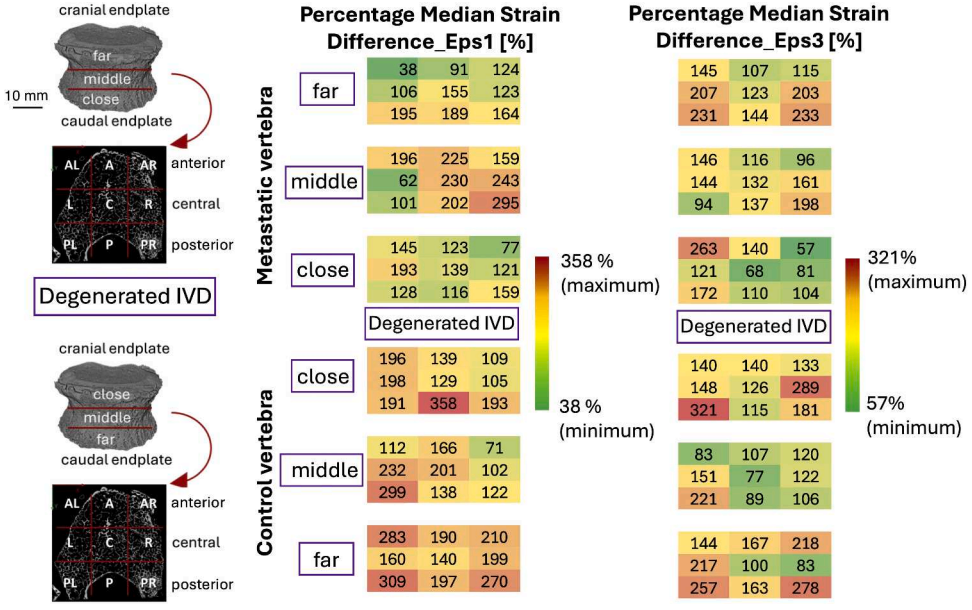

Fig. 5. Median values of the subROI Percentage Median Strain Difference (PMSD) evaluated in the five metastatic (top) and five control (bottom) vertebrae, for Eps1 (left) and Eps3 (right). The PMSD values are reported from the minimum (green) to the maximum (red).

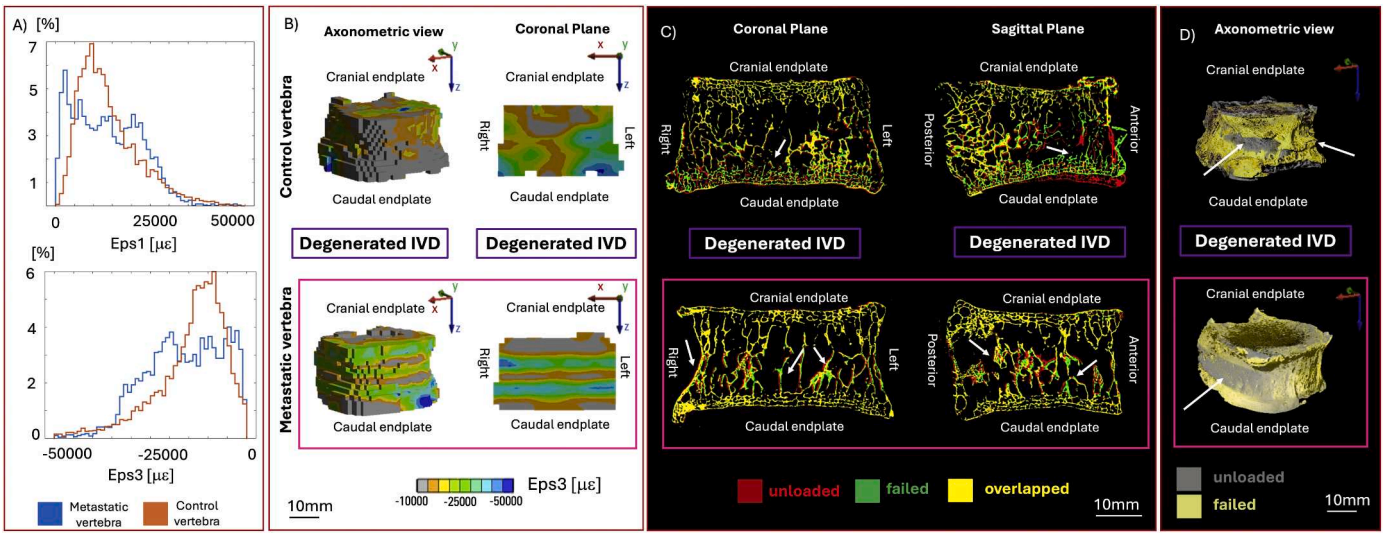

Fig. 6. Example of a spine segment (Specimen ID4): consisting of a control (radiologically healthy) and a metastatic vertebra. A) Frequency plots of Eps1 (top) and Eps 3 (bottom) are reported, splitting between the metastatic (orange) and the control (blue) vertebrae. B) 3D colour maps of Eps3 beyond −10000 με in axonometric view and in the coronal (xy) plane. The degenerated IVD is highlighted by the purple square and the failed vertebra is highlighted by the pink square. C) μCT scans of the vertebrae before (red) and after (green) failure are overlapped (yellow) in order to highlight the failure location in the coronal (xy) and sagittal (yz) plane. White arrows highlight the failed regions. D) 3D μCT scans of the vertebrae before (grey) and after (yellow) failure are overlapped in order to highlight the failure location. White arrows highlight the failed regions.

measured in metastatic and control vertebrae. As explained in previous studies [14,15], every metastatic lesion affects differently the vertebra strains in function of its type, size and position, inducing unique local strain distribution. Therefore, the effects of lesions should be observed in individual vertebrae (See Supplementary Materials).

In the case of control vertebrae in intact condition, the optimized microstructure enabled a uniform strain distribution in the vertebral body, with consequent low heterogeneity of the strain field. This has already been shown by experimental strain measurements performed on the cortical shells with strain gauges [17,70]. By contrast, after the degeneration of the IVD, the different load transferred to the vertebral body changed the resistance of the trabecular bone, not optimised for this loading condition. This created high heterogeneity in the strain field within the vertebral body, which, *in vivo* in the long term, may lead to sub-optimal bone remodelling [71]. Within metastatic vertebrae, the bone trabecular microstructure was partially compromised by the lytic lesions even in the intact condition where high strain heterogeneity was observed, especially in or close to the lytic defects [14,15]. In the degenerated condition, this scenario was worsened, with peak maximum and minimum principal strains close to failure even when loaded with the lowest load step (nominally designed to induce deformations in the elastic regime in intact condition). This result highlighted the potential synergistic destabilising effects of IVD degeneration and metastatic lesions on the vertebral bone microstructure.

In both control and metastatic vertebrae in degenerated condition, the strain increased substantially in peripheral regions [29,32] rather than in the centre of the vertebral body or of the endplates [15,72]. Indeed, the loss of hydration and pressure inside the NP [23,25,27,31,73,74] was previously reported to concentrate the load onto the posterior half of the vertebra, shifting the load from the inner NP to the outer AF and, as a consequence, from the inner portion of the endplate to the outer cortical shell of the vertebra [31]. This effect was observed in the central (C) subROIs of the vertebrae, anatomically in correspondence to the NP, that exhibited a moderate increase in the absolute values of Eps1 and Eps3 after IVD degeneration compared to the other subROIs. Conversely, the outer subROIs, anatomically associated with the AF, experienced the largest increase in absolute Eps1 and Eps3 values, after IVD degeneration (Fig. 5). Indeed, while, in the intact condition, strain concentrations were associated with the position of the lytic metastases (i.e. in the trabecular bone, without affecting the cortical shell of the vertebral body), in degenerated condition strain concentrations were localised also in the outer subROIs of the metastatic vertebral body. Moreover, it should be noted that these peck strains were localised in the regions that failed, as observed from the following load step at failure.

Degeneration of the IVDs also affected the mechanical behaviour of vertebrae with and without metastases at failure. In the current study, four metastatic (80 %, ID2, ID3, ID4, ID5) and one control vertebra (20 %, ID4) exhibited large strains and failed at the mid-height of the vertebral body, without affecting the endplates. This behaviour was clearly different from that of spine segments, with or without lesions, and loaded through non-degenerated IVDs [15,75–79]. In fact, when the IVD is not degenerated the majority of the applied load is transferred through the NP and leads to protrusion of the NP into the adjacent vertebra, which leads to endplate damage and is likely to occur in fractures induced by compression and compression-flexion [78,80]. In particular, in cases of metastatic spine segments without degenerated IVD, failure was found to involve the endplates and the underlying trabecular bone, with larger strains usually observed in metastatic vertebrae (close to the lytic or mixed metastases) compared to the radiologically healthy controls [15]. As a confirmation of this behaviour, in this study, two endplate regions (in ID1, Fig. S3, the superior endplate of the metastatic vertebra, and in ID3, Fig. S5, the superior endplate of the control vertebra) adjacent to non-degenerated IVD failed showing a clear collapse of the endplate and of the underneath trabecular tissue, similarly to what was previously observed [15,81]. Conversely, in the case of degenerated IVDs, the load distribution was more isotropic and the majority of the applied load was transferred through the periphery of the endplate [27]. As a consequence, the trabecular pattern and the curvature of the cortical shell led to a larger deformation (both Eps1 and Eps3) at the mid-height of the vertebral body of the control and metastatic vertebrae (regardless of the position of the metastasis), leading to transverse fractures [75,76] (Fig. 6, 7). Indeed, Eps1 and Eps3 in vertebrae with lytic metastases and control vertebrae were not significantly different and ranged similarly. Strain peaks and regions with strain concentrations were mainly observed in vertebrae with metastases rather than in the adjacent controls, at the mid-height of the vertebral body and in correspondence with the lytic lesions (Fig. S4, S5, S6). However, despite the lower magnitude and the

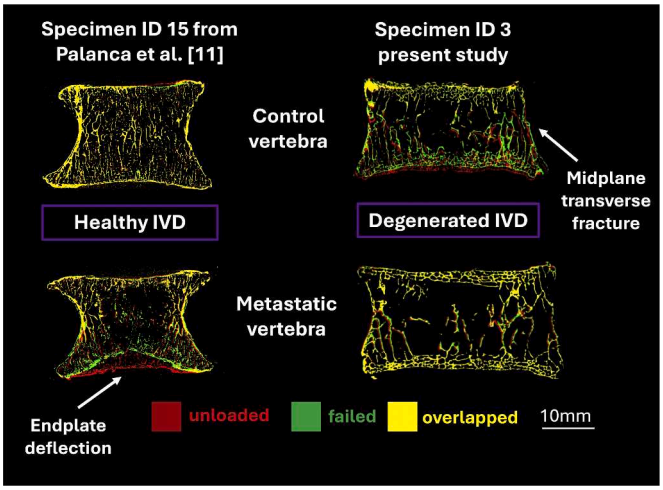

Fig. 7. Examples of different failures. Left: failure involving the tissue close to the endplate and the deflection of the endplate in a vertebra with lytic metastases adjacent to a healthy IVD (specimen tested in [15], not reported here). The health status of the IVDs was evaluated using the scoring systems proposed by [47,85]: each specimen exhibited no or mild degeneration of the central IVD. Right: Failure involving the cortical shell and the midplane of the vertebra in a control vertebra adjacent to a degenerated IVD. Unloaded condition in red colour, failed condition in green colour, overlap in yellow colour.

smaller region affected, also control vertebrae exhibited deformations larger than the bone failure strain in the middle region of the vertebral body and close to the cortical shell. To the best of the authors' knowledge, the involvement of the cortical shell in the failure process has been reported only for transcortical metastatic defects [82–84] and the transverse fracture through the whole vertebra, in its midplane, is reported by Brinckmann et al. [76] as an exception. On the contrary, this study demonstrated the occurrence of transverse fractures in both control and metastatic vertebrae adjacent to degenerated IVDs due to failure of the vertical trabeculae and of the cortical shell, leading to a shift of the endplate and a loss of vertebrae height. These results highlighted the impact of IVD degeneration on the redistribution of the loads between the NP and the AF of the disc, and therefore, between the dense mesh of trabecular bone locally affected by the metastases and the thin cortical bone of the vertebral body.

This study has some limitations worth clarifying. Puncturing and enzymatic degeneration emulate in a controlled and reproducible way the IVD degeneration but, like any *ex vivo* models, cannot completely replicate the complex mechanisms underpinning human IVD degeneration. The induction of mock degeneration with collagenase digestion demonstrated induction of fissures and decreased matrix staining with histology. However, histological grading of tissues was not possible as all IVDs had been loaded up to failure prior to histological assessment and thus grading of histology was not appropriate. Whilst histological grading of degeneration alone without load would have been beneficial to confirm the degeneration model, this would have required additional human samples which are a scarce resource, and the induction of degeneration with collagenase has been reported previously in *ex vivo* animal disc models [50,86]. The effects of the enzymatic degeneration in the tested specimens were assessed in two out of five specimens through a visual investigation for the identification of the key features of demarcation and fissures, and the absence of the gelatinous NP, typical of a degenerated disc [22]. While *in vivo* IVD degeneration is typically associated with bony sclerosis and remodelling [21,87] as a consequence of the different load sharing, this process could not be replicated in the rapid *ex vivo* model used in this study [71,88]. Despite this, the findings of the study are still valuable since the specimens used in this study were affected by a systematic disease (i.e. lytic bone metastases), which led to the disruption of the bone homeostasis and the optimized trabecular pattern [7], without being driven by a mechanical adaptation.

The number of specimens is limited. However, to perform a comparative paired strain analysis, increasing the statistical power to generalize the findings, the same control and metastatic vertebral bodies were tested with initially intact IVD and then after the IVD degeneration. Each specimen in the initial condition acted as its own control. Thus, the differences in strains observed in the comparison before and after degeneration were due only to the degeneration of the IVD. Moreover, data robustness was confirmed by the power analysis. Whereby, setting alpha (type I error) = 0.05, beta (type II error) = 20 %, effect size (differences between degenerated and not degenerated specimens) = 2000 με, and standard deviation of the group (the overall uncertainty) = 500 με, the minimum sample size requested for paired analysis was 3.

Due to the relatively small field of view of the μCT scanner, it was possible to test only vertebrae of relatively small size, such as thoracic vertebrae, without the posterior arches. Despite the anatomical change and the loss of the mechanical contribution of the posterior element and the facet joints in axial compression, under physiological loading conditions, only a small portion of the load is borne by the posterior elements [89,90]. However, the interaction of IVD degeneration and removal of the posterior elements might change the strain distribution in the vertebrae.

Unfortunately, investigation of the mechanical behaviour of both the hard (i.e. vertebrae) and soft (i.e. IVDs) tissues at the same time was not possible. Indeed, μCT enables imaging of mineralised tissues such as metastatic and control vertebrae. The analysis of the effects of bone metastases on the mechanical behaviour of healthy and degenerated IVDs can be performed through different and more time consuming imaging modalities (phase contrast or combination with MRI [23]) and would affect dramatically this *in situ* mechanical testing procedure.

Axial compression is the loading condition for which the vertebra is optimized, and the major load direction in physiological conditions (i.e. standing) [70]. However, more realistic loading conditions, such as cyclic flexion/extension or torsion, should be further investigated in future studies to confirm the findings of this study. Moreover, to accurately simulate the clinical scenario involving simultaneous IVD degeneration and bone metastases, lumbar spine segments should be included in future studies.

Finally, in this study, the loading rate was slower than that usually associated with vertebral fractures (approximately 16000 Ns^{-1}) suggesting other possible injury mechanisms [91,92].

5. Conclusion

This study highlighted the relationship between IVD degeneration and the mechanical behaviour of metastatic and radiologically healthy human vertebrae. The level of disc degeneration is a key factor in determining the failure mode and location of metastatic spine segments. Indeed, non-degenerated IVDs may induce burst fracture or endplate damage in healthy or metastatic vertebrae. Conversely, IVD degeneration causes transverse fracture in the vertebrae involving the middle portion of the vertebral body and fracture of the cortical shell. These results suggest the clinical relevance of introducing MRI imaging and the evaluation of the IVD level of degeneration in the clinical routine to assess the risk of spinal instability and fracture and to best stratify neoplastic patients for treatments.

Funding sources

The study was partially supported by the AO Spine Knowledge Forum Associate Research Award (AOS-KF-TUM-22–003), Marie Skłodowska-Curie Individual Fellowship (MetaSpine, MSCA- IFEF-ST, 832430/2018) and by the METASTRA project (EU H2022 grant ID 101080135; UK Horizon Europe Guarantee Extension ID: 10075325).

CRediT authorship contribution statement

Giulia Cavazzoni: Writing – original draft, Methodology, Investigation, Formal analysis, Data curation, Conceptualization. **Margherita Pasini:** Writing – review & editing, Investigation. **Christine L. Le Maitre:** Writing – review & editing, Supervision, Resources, Methodology, Conceptualization. **Enrico Dall'Ara:** Writing – review & editing, Supervision, Resources, Methodology, Conceptualization. **Marco Palanca:** Writing – review & editing, Supervision, Methodology, Investigation, Funding acquisition, Formal analysis, Conceptualization.

Declaration of competing interests

The authors declare the following financial interests/personal relationships which may be considered as potential competing interests: Marco Palanca reports financial support was provided by AO Foundation. Marco Palanca reports financial support was provided by European Commission Marie Sklodowska-Curie Actions. Marco Palanca reports financial support was provided by Horizon Europe. Enrico Dall'Ara reports financial support was provided by Horizon Europe. If there are other authors, they declare that they have no known competing financial interests or personal relationships that could have appeared to influence the work reported in this paper.

Acknowledgements

We would like to thank Prof. Luca Cristofolini for the kind support and contribution given in this work; Dr. Giovanni Barbanti-Bròdano and Dr. Paolo Luzi for helping in the specimen classification and selection, Dr. Joseph Snuggs and Ms Orla Gallagher for the help with the enzymatic degeneration and histology analysis; Camilla Morbidelli and Erica Turchi for their smart programming skills.

Supplementary materials

Supplementary material associated with this article can be found, in the online version, at doi:10.1016/j.actbio.2025.01.018.

References

[1] G. Selvaggi, G.V. Scagliotti, Management of bone metastases in cancer: a review, Crit. Rev. Oncol. Hematol. 56 (2005) 365–378, https://doi.org/10.1016/j.critrevonc.2005.03.011.

[2] R.E. Coleman, Clinical features of metastatic bone disease and risk of skeletal morbidity, Clin. Cancer Res. 12 (2006) 6243s–6249s, https://doi.org/10.1158/1078-0432.CCR-06-0931.

[3] R.E. Coleman, P.I. Croucher, A.R. Padhani, P. Clézardin, E. Chow, M. Fallon, T. Guise, S. Colangeli, R. Capanna, L. Costa, Bone metastases, Nat. Rev. Dis. Primers. 6 (2020) 83, https://doi.org/10.1038/s41572-020-00216-3.

[4] P. Sutcliffe, M. Connock, D. Shyangdan, R. Court, N.-B. Kandala, A. Clarke, A systematic review of evidence on malignant spinal metastases: natural history and technologies for identifying patients at high risk of vertebral fracture and spinal cord compression, Health Technol. Assess. 17 (2013), https://doi.org/10.3310/hta17420.

[5] S. Bailey, M.A. Stadelmann, P.K. Zysset, D. Vashishth, R.N. Alkalay, Influence of metastatic bone lesion type and tumor origin on human vertebral bone architecture, matrix quality, and mechanical properties, J of Bone & Mineral Res 37 (2022) 896–907, https://doi.org/10.1002/jbmr.4539.

[6] G. Cavazzoni, L. Cristofolini, E. Dall'Ara, M. Palanca, Bone metastases do not affect the measurement uncertainties of a global digital volume correlation algorithm, Front. Bioeng. Biotechnol. 11 (2023) 1152358, https://doi.org/10.3389/fbioe.2023.1152358.

[7] G. Cavazzoni, E. Dall'Ara, M. Palanca, Microstructure of the human metastatic vertebral body, Front Endocrinol 15 (2025) 1508504, https://doi.org/10.3389/fendo.2024.1508504.

[8] R. Van Den Brande, E. Mj Cornips, M. Peeters, P. Ost, C. Billiet, E. Van De Kelft, Epidemiology of spinal metastases, metastatic epidural spinal cord compression and pathologic vertebral compression fractures in patients with solid tumors: a systematic review, J. Bone Oncol. 35 (2022) 100446, https://doi.org/10.1016/j.jbo.2022.100446.

[9] R.U. Ashford, R.L. Randall, Bone metastases: epidemiology and societal effect, in: R.L. Randall (Ed.), Metastatic bone disease, Springer New York, New York, NY, 2016: pp. 3–11. https://doi.org/10.1007/978-1-4614-5662-9_1.

[10] M. Campos, J. Urrutia, T. Zamora, J. Román, V. Canessa, Y. Borghero, A. Palma, M. Molina, The spine instability neoplastic score: an independent reliability and reproducibility analysis, Spine J. 14 (2014) 1466–1469, https://doi.org/10.1016/j.spinee.2013.08.044.

[11] L. Bollen, K. Groenen, W. Pondaag, C.S.P. van Rijswijk, M. Fiocco, Y.M. Van der Linden, S.P.D. Dijkstra, Clinical evaluation of the spinal instability neoplastic score in patients treated with radiotherapy for symptomatic spinal bone metastases, Spine (Phila Pa 1976) 42 (2017) E956–E962, https://doi.org/10.1097/BRS.0000000000002058.

[12] C.G. Fisher, C.P. DiPaola, T.C. Ryken, M.H. Bilsky, C.I. Shaffrey, S.H. Berven, J. S. Harrop, M.G. Fehlings, S. Boriani, D. Chou, M.H. Schmidt, D.W. Polly, R. Biagini, S. Burch, M.B. Dekutoski, A. Ganju, P.C. Gerszten, Z.L. Gokaslan, M.W. Groff, N. J. Liebsch, E. Mendel, S.H. Okuno, S. Patel, L.D. Rhines, P.S. Rose, D.M. Sciubba, N. Sundaresan, K. Tomita, P.P. Varga, L.R. Vialle, F.D. Vrionis, Y. Yamada, D. R. Fourney, A novel classification system for spinal instability in neoplastic disease: an evidence-based approach and expert consensus from the spine oncology study group, Spine (Phila Pa 1976) 35 (2010) E1221–E1229, https://doi.org/10.1097/BRS.0b013e3181e16ae2.

[13] M.A. Stadelmann, D.E. Schenk, G. Maquer, C. Lenherr, F.M. Buck, D.D. Bosshardt, S. Hoppe, N. Theumann, R.N. Alkalay, Philippe K. Zysset, Conventional finite element models estimate the strength of metastatic human vertebrae despite alterations of the bone's tissue and structure, Bone 141 (2020) 115598, https://doi.org/10.1016/j.bone.2020.115598.

[14] M. Palanca, G. Barbanti-Bròdano, D. Marras, M. Marciante, M. Serra, A. Gasbarrini, E. Dall'Ara, L. Cristofolini, Type, size, and position of metastatic lesions explain the deformation of the vertebrae under complex loading conditions, Bone 151 (2021) 116028, https://doi.org/10.1016/j.bone.2021.116028.

[15] M. Palanca, G. Cavazzoni, E. Dall'Ara, The role of bone metastases on the mechanical competence of human vertebrae, Bone 173 (2023) 116814, https://doi.org/10.1016/j.bone.2023.116814.

[16] M.C. Costa, L.B. Bresani Campello, M. Ryan, J. Rochester, M. Viceconti, E. Dall'Ara, Effect of size and location of simulated lytic lesions on the structural properties of human vertebral bodies, a micro-finite element study, Bone Rep. 12 (2020) 100257, https://doi.org/10.1016/j.bonr.2020.100257.

[17] V. Danesi, P. Erani, N. Brandolini, M.M. Juszczyk, L. Cristofolini, Effect of the In Vitro boundary conditions on the surface strain experienced by the vertebral body in the elastic regime, J. Biomech. Eng. 138 (2016) 104503, https://doi.org/10.1115/1.4034383.

[18] A.I. Hussein, Z.D. Mason, E.F. Morgan, Presence of intervertebral discs alters observed stiffness and failure mechanisms in the vertebra, J. Biomech. 46 (2013) 1683–1688, https://doi.org/10.1016/j.jbiomech.2013.04.004.

[19] M.A. Adams, D.S. Mcnally, P. Dolan, Stress distributions inside intervertebral discs. The effects of age and degeneration, JBJS 78 (1996), https://doi.org/10.1302/0301-620×78b6.1287.

[20] M.A. Adams, P.J. Roughley, What is intervertebral disc degeneration, and what causes it?: Spine (Phila Pa 1976) 31 (2006) 2151–2161, https://doi.org/10.1097/01.brs.0000231761.73859.2c.

[21] C.L. Le Maitre, C.L. Dahia, M. Giers, S. Illien-Junger, C. Cicione, D. Samartzis, G. Vadala, A. Fields, J. Lotz, Development of a standardized histopathology scoring system for human intervertebral disc degeneration: an Orthopaedic research society spine section initiative, JOR. Spine 4 (2021) e1167, https://doi.org/10.1002/jsp2.1167.

[22] J.P. Urban, S. Roberts, Degeneration of the intervertebral disc, Arthritis Res. Ther. 5 (2003) 120, https://doi.org/10.1186/ar629.

[23] S. Tavana, S.D. Masouros, N. Baxan, B.A. Freedman, U.N. Hansen, N. Newell, The effect of degeneration on internal strains and the mechanism of failure in human intervertebral discs analyzed using digital volume correlation (DVC) and ultra-high field MRI, Front. Bioeng. Biotechnol. 8 (2021) 610907, https://doi.org/10.3389/fbioe.2020.610907.

[24] C. Liebsch, H.-J. Wilke, Even mild intervertebral disc degeneration reduces the flexibility of the thoracic spine: an experimental study on 95 human specimens, Spine J. 22 (2022) 1913–1921, https://doi.org/10.1016/j.spinee.2022.06.010.

[25] G.D. O'Connell, E.J. Vresilovic, D.M. Elliott, Human intervertebral disc internal strain in compression: the effect of disc region, loading position, and degeneration, J. Orthopaedic Res. 29 (2011) 547–555, https://doi.org/10.1002/jor.21232.

[26] N. Tanaka, H.S. An, T.-H. Lim, A. Fujiwara, C.-H. Jeon, V.M. Haughton, The relationship between disc degeneration and flexibility of the lumbar spine, The Spine J. 1 (2001) 47–56, https://doi.org/10.1016/S1529-9430(01)00006-7.

[27] T.S. Keller, T. Hansson, A.C. Abram, D.M. Spengler, M.M. Panjabi, Regional variations in the compressive properties of lumbar vertebral trabeculae, Effect. Disc Degenerat., Spine (1989) 14, https://doi.org/10.1097/00007632-198909000-00016.

[28] A.L. Parmenter, E. Newham, A. Sharma, C.M. Disney, H. Deyhle, F. Bosi, N.J. Terrill, B.K. Bay, A.A. Pitsillides, H.S. Gupta, P.D. Lee, Multimodal imaging reveals multiscale mechanical interplay in vertebral endplate microarchitecture during intervertebral disc loading, (2024). 10.1101/2024.08.19.608559.

[29] L. Dai, The relationship between vertebral body deformity and disc degeneration in lumbar spine of the senile, Eur. Spine J. 7 (1998) 40–44, https://doi.org/10.1007/s005860050025.

[30] A. Polikeit, L.P. Nolte, S.J. Ferguson, Simulated influence of osteoporosis and disc degeneration on the load transfer in a lumbar functional spinal unit, J. Biomech. 37 (2004) 1061–1069, https://doi.org/10.1016/j.jbiomech.2003.11.018.

[31] J. Homminga, H. Weinans, W. Gowin, D. Felsenberg, R. Huiskes, Osteoporosis changes the amount of vertebral trabecular bone at risk of fracture but not the vertebral load distribution, Spine (Phila Pa 1976) 26 (2001) 1555–1560, https://doi.org/10.1097/00007632-200107150-00010.

[32] K.A. Raftery, A. Kargarzadeh, S. Tavana, N. Newell, Disc degeneration influences the strain magnitude and stress distribution within the adjacent trabecular bone, Front. Bioeng. Biotechnol. (2024) 12, https://doi.org/10.3389/fbioe.2024.1511685.
[33] D. Resnick, G. Niwayama, Intervertebral disc abnormalities associated with vertebral metastasis: observations in patients and cadavers with prostatic cancer, Invest. Radiol. 13 (1977) 182–190, https://doi.org/10.1097/00004424-197805000-00002.
[34] P.N.M. Tyrrell, V.N. Cassar-Pullicino, R.K. Lalam, B.J. Tins, Bone Metastases 1: Spine, in: A.M. Davies, M. Sundaram, S.L.J. James (Eds.), Imaging of Bone Tumors and Tumor-Like Lesions, Springer Berlin Heidelberg, Berlin, Heidelberg, 2009: pp. 461–479. 10.1007/978-3-540-77984-1_26.
[35] M. Teraguchi, N. Yoshimura, H. Hashizume, S. Muraki, H. Yamada, A. Minamide, H. Oka, Y. Ishimoto, K. Nagata, R. Kagotani, N. Takiguchi, T. Akune, H. Kawaguchi, K. Nakamura, M. Yoshida, Prevalence and distribution of intervertebral disc degeneration over the entire spine in a population-based cohort: the Wakayama Spine Study, OsteoArthritis Cartilage 22 (2014) 104–110, https://doi.org/10.1016/j.joca.2013.10.019.
[36] D.D. Hubbard, D.R. Gunn, Secondary carcinoma of the spine with destruction of the intervertebral disk, Clin. Orthop. Relat. Res. 88 (1972), https://doi.org/10.1097/00003086-197210000-00016.
[37] T. Yasuma, Y. Yamauchi, K. Arai, E. Makino, Histopathologic study on tumor infiltration into the intervertebral disc, Spine (Phila Pa 1976) 14 (1989), https://doi.org/10.1097/00007632-198911000-00018.
[38] Y. Kakitsubata, D.J. Theodorou, S.J. Theodorou, K. Nabeshima, S. Tamura, Metastatic disease involving the discovertebral junction of the spine, Joint. Bone Spine 76 (2009) 50–56, https://doi.org/10.1016/j.jbspin.2008.03.007.
[39] M.K. Ryan, S. Oliviero, M.C. Costa, J.M. Wilkinson, E. Dall'Ara, Heterogeneous strain distribution in the subchondral bone of human osteoarthritic femoral heads, measured with digital volume correlation, Materials (Basel) 13 (2020) 4619, https://doi.org/10.3390/ma13204619.
[40] M. Palanca, G. De Donno, E. Dall'Ara, A novel approach to evaluate the effects of artificial bone focal lesion on the three- dimensional strain distributions within the vertebral body, PLoS. One 16 (2021) 1–16, https://doi.org/10.1371/journal.pone.0251873.
[41] V. Danesi, L. Zani, A. Scheele, F. Berra, L. Cristofolini, Reproducible reference frame for in vitro testing of the human vertebrae, J. Biomech. 47 (2014) 313–318, https://doi.org/10.1016/j.jbiomech.2013.10.005.
[42] N. Newell, J. Little, A. Christou, M. Adams, C. Adam, S. Masouros, Biomechanics of the human intervertebral disc: a review of testing techniques and results, J. Mech. Behav. Biomed. Mater. 69 (2017) 420–434, https://doi.org/10.1016/j.jmbbm.2017.01.037.
[43] J.S. Tan, S. Uppuganti, Cumulative multiple freeze-thaw cycles and testing does not affect subsequent within-day variation in intervertebral flexibility of human cadaveric lumbosacral spine, Spine (Phila Pa 1976) 37 (2012) E1238–E1242, https://doi.org/10.1097/BRS.0b013e31826111a3.
[44] H.Demirturk Kocasarac, E.S. Kursun-Cakmak, G. Ustaoglu, S. Bayrak, K. Orhan, M. Noujeim, Assessment of signal-to-noise ratio and contrast-to-noise ratio in 3 T magnetic resonance imaging in the presence of zirconium, titanium, and titanium-zirconium alloy implants, Oral Surg. Oral Med. Oral Pathol. Oral Radiol. 129 (2020) 80–86, https://doi.org/10.1016/j.oooo.2019.08.020.
[45] A.S. Shatil, K.M. Matsuda, C.R. Figley, A method for whole brain Ex Vivo magnetic resonance imaging with minimal susceptibility artifacts, Front. Neurol. 7 (2016), https://doi.org/10.3389/fneur.2016.00208.
[46] C.W.A. Pfirrmann, A. Metzdorf, M. Zanetti, J. Hodler, N. Boos, Magnetic resonance classification of lumbar intervertebral disc degeneration, Spine (Phila Pa 1976) 26 (2001) 1873–1878, https://doi.org/10.1097/00007632-200109010-00011.
[47] C. Liebsch, Y. Tao, A. Kienle, H.-J. Wilke, Validity and interobserver agreement of a new radiographic grading system for intervertebral disc degeneration: part III. Thoracic spine, Eur. Spine J. 31 (2022) 726–734, https://doi.org/10.1007/s00586-021-06970-6.
[48] M.E. Kunkel, A. Herkommer, M. Reinehr, T.M. Böckers, H.-J. Wilke, Morphometric analysis of the relationships between intervertebral disc and vertebral body heights: an anatomical and radiographic study of the human thoracic spine: morphometric analysis of the relationships between intervertebral disc and vertebral body heights, J. Anat. 219 (2011) 375–387, https://doi.org/10.1111/j.1469-7580.2011.01397.x.
[49] M.M. Panjabi, K. Takata, V. Goel, D. Federico, T. Oxland, J. Duranceau, M. Krag, Thoracic human vertebrae. Quantitative three-dimensional anatomy, Spine (Phila Pa 1976) 16 (1991) 888–901, https://doi.org/10.1097/00007632-199108000-00006.
[50] C. Rustenburg, J. Snuggs, K. Emanuel, A. Thorpe, C. Sammon, C. Le Maitre, T. Smit, Modelling the catabolic environment of the moderately degenerated disc with a caprine ex vivo loaded disc culture system, eCM 40 (2020) 21–37, https://doi.org/10.22203/eCM.v040a02.
[51] E.D. Rivera Tapia, J.R. Meakin, T.P. Holsgrove, In-vitro models of disc degeneration – a review of methods and clinical relevance, J. Biomech. 142 (2022), https://doi.org/10.1016/j.jbiomech.2022.111260.
[52] J. Antoniou, F. Mwale, C.N. Demers, G. Beaudoin, T. Goswami, M. Aebi, M. Alini, Quantitative magnetic resonance imaging of enzymatically induced degradation of the nucleus Pulposus of intervertebral discs, Spine (Phila Pa 1976) 31 (2006) 1547–1554, https://doi.org/10.1097/01.brs.0000221995.77177.9d.
[53] A. Barbir, A.J. Michalek, R.D. Abbott, J.C. Iatridis, Effects of enzymatic digestion on compressive properties of rat intervertebral discs, J. Biomech. 43 (2010) 1067–1073, https://doi.org/10.1016/j.jbiomech.2009.12.005.
[54] S. Basatvat, F.C. Bach, M.N. Barcellona, A.L. Binch, C.T. Buckley, B. Bueno, N. O. Chahine, A. Chee, L.B. Creemers, S. Dudli, B. Fearing, S.J. Ferguson, J. Gansau, B. Gantenbein, R. Gawri, J.D. Glaeser, S. Grad, J. Guerrero, L. Haglund, P. A. Hernandez, J.A. Hoyland, C. Huang, J.C. Iatridis, S. Illien-Junger, L. Jing, P. Kraus, L.T. Laagland, G. Lang, V. Leung, Z. Li, T. Lufkin, J.C. Van Maanen, E. E. McDonnell, C.J. Panebianco, S.M. Presciutti, S. Rao, S.M. Richardson, S. Romereim, T.C. Schmitz, J. Schol, L. Setton, D. Sheyn, J.W. Snuggs, Y. Sun, X. Tan, M.A. Tryfonidou, N. Vo, D. Wang, B. Williams, R. Williams, S.T. Yoon, C. L. Le Maitre, Harmonization and standardization of nucleus pulposus cell extraction and culture methods, JOR. Spine 6 (2023) e1238, https://doi.org/10.1002/jsp2.1238.
[55] A.A. Thorpe, V.L. Boyes, C. Sammon, C.L. Le Maitre, Thermally triggered injectable hydrogel, which induces mesenchymal stem cell differentiation to nucleus pulposus cells: potential for regeneration of the intervertebral disc, Acta Biomater 36 (2016) 99–111, https://doi.org/10.1016/j.actbio.2016.03.029.
[56] S.C. Cowin, ed., Bone mechanics handbook, in: Bone Mechanics Handbook, 2nd ed., CRC Press, 2001: pp. 183–206. 10.1201/b14263-11.
[57] P.J. Ehrlich, L.E. Lanyon, Mechanical strain and bone cell function: a review, Osteoporos. Int. 13 (2002) 688–700, https://doi.org/10.1007/s001980200095.
[58] L.E. Lanyon, Functional strain in bone tissue as an objective and controlling stimulus for adaptive bone remodelling, J. Biomech. 20 (1987) 1093–1098, https://doi.org/10.1016/0021-9290(87)90026-1.
[59] G.J. Kazakia, A.J. Burghardt, S. Cheung, S. Majumdar, Assessment of bone tissue mineralization by conventional x-ray microcomputed tomography: comparison with synchrotron radiation microcomputed tomography and ash measurements: assessment of bone tissue mineralization by microcomputed tomography, Med. Phys. 35 (2008) 3170–3179, https://doi.org/10.1118/1.2924210.
[60] E. Dall'Ara, D. Barber, M. Viceconti, About the inevitable compromise between spatial resolution and accuracy of strain measurement for bone tissue: a 3D zero-strain study, J. Biomech. 47 (2014) 2956–2963, https://doi.org/10.1016/j.jbiomech.2014.07.019.
[61] D. Barber, D. Hose, Automatic segmentation of medical images using image registration: diagnostic and simulation applications, J. Med. Eng. Technol. 29 (2005) 53–63, https://doi.org/10.1080/03091900412331289889.
[62] M. Palanca, G. Tozzi, L. Cristofolini, M. Viceconti, E. Dall'Ara, Three-dimensional local measurements of bone strain and displacement: comparison of three digital volume correlation approaches, J. Biomech. Eng. 137 (2015) 071006, https://doi.org/10.1115/1.4030174.
[63] D.C. Barber, E. Oubel, A.F. Frangi, D.R. Hose, Efficient computational fluid dynamics mesh generation by image registration, Med. Image Anal. 11 (2007) 648–662, https://doi.org/10.1016/j.media.2007.06.011.
[64] E. Dall'Ara, M. Peña-Fernández, M. Palanca, M. Giorgi, L. Cristofolini, G. Tozzi, Precision of digital volume correlation approaches for strain analysis in bone imaged with micro-computed tomography at different dimensional levels, Front. Mater. 4 (2017) 31, https://doi.org/10.3389/fmats.2017.00031.
[65] L. Liu, E.F. Morgan, Accuracy and precision of digital volume correlation in quantifying displacements and strains in trabecular bone, J. Biomech. 40 (2007) 3516–3520, https://doi.org/10.1016/j.jbiomech.2007.04.019.
[66] A.I. Hussein, E.F. Morgan, The effect of intravertebral heterogeneity in microstructure on vertebral strength and failure patterns, Osteoporos. Int. 24 (2013) 979–989, https://doi.org/10.1007/s00198-012-2039-1.
[67] The jamovi project, jamovi (Version 2.3), (2023). https://www.jamovi.org.
[68] E.F. Morgan, T.M. Keaveny, Dependence of yield strain of human trabecular bone on anatomic site, J. Biomech. 34 (2001) 569–577, https://doi.org/10.1016/S0021-9290(01)00011-2.
[69] U. Nöth, A.M. Osyczka, R. Tuli, N.J. Hickok, K.G. Danielson, R.S. Tuan, Multilineage mesenchymal differentiation potential of human trabecular bone-derived cells, J. Orthopaedic Res. 20 (2002) 1060–1069, https://doi.org/10.1016/S0736-0266(02)00018-9.
[70] L. Cristofolini, In vitro evidence of the structural optimization of the human skeletal bones, J. Biomech. 48 (2015) 787–796, https://doi.org/10.1016/j.jbiomech.2014.12.010.
[71] E.K. Simpson, I.H. Parkinson, B. Manthey, N.L. Fazzalari, Intervertebral disc disorganization is related to trabecular bone architecture in the lumbar Spine, J Bone Mineral Res 16 (2001) 681–687, https://doi.org/10.1359/jbmr.2001.16.4.681.
[72] T.M. Jackman, A.I. Hussein, A.M. Adams, K.K. Makhnejia, E.F. Morgan, Endplate deflection is a defining feature of vertebral fracture and is associated with properties of the underlying trabecular bone, J. Orthopaedic Res. 32 (2014) 880–886, https://doi.org/10.1002/jor.22620.
[73] S.K. Eswaran, A. Gupta, M.F. Adams, T.M. Keaveny, Cortical and trabecular load sharing in the human vertebral body, J. Bone Mineral Res. 21 (2006) 307–314, https://doi.org/10.1359/jbmr.2006.21.2.307.
[74] S.J. Ferguson, T. Steffen, Biomechanics of the aging spine, Eur. Spine J. 12 (2003) S97–S103, https://doi.org/10.1007/s00586-003-0621-0.
[75] T. Hansson, B. Roos, The relation between bone mineral content, experimental compression fractures, and disc degeneration in lumbar vertebrae, Spine (Phila Pa 1976) 6 (1981), https://doi.org/10.1097/00007632-198103000-00007.
[76] P. Brinckmann, M. Biggemann, D. Hilweg, Prediction of the compressive strength of human lumbar vertebrae, Clin. Biomech. 2 (1989), https://doi.org/10.1016/0268-0033(89)90071-5.
[77] P.A. Hulme, S.J. Ferguson, S.K. Boyd, Determination of vertebral endplate deformation under load using micro-computed tomography, J. Biomech. 41 (2008) 78–85. https://doi.org/10.1016/j.jbiomech.2007.07.018..

[78] R.L. Ferguson, B.L. Allen, A mechanistic classification of thoracolumbar spine fractures, Clin. Orthop. Relat. Res. 189 (1984) 77–88, https://doi.org/10.1097/00003086-198410000-00009.
[79] T.M. Jackman, A.M. DelMonaco, E.F. Morgan, Accuracy of finite element analyses of CT scans in predictions of vertebral failure patterns under axial compression and anterior flexion, J. Biomech. 49 (2016) 267–275, https://doi.org/10.1016/j.jbiomech.2015.12.004.
[80] G.T. Desmoulin, V. Pradhan, T.E. Milner, Mechanical aspects of intervertebral disc injury and implications on biomechanics, Spine (Phila Pa 1976) 45 (2020) E457–E464, https://doi.org/10.1097/BRS.0000000000003291.
[81] F.-D. Zhao, P. Pollintine, B.D. Hole, M.A. Adams, P. Dolan, Vertebral fractures usually affect the cranial endplate because it is thinner and supported by less-dense trabecular bone, Bone 44 (2009) 372–379, https://doi.org/10.1016/j.bone.2008.10.048.
[82] R.N. Alkalay, Effect of the metastatic defect on the structural response and failure process of human vertebrae: an experimental study, Clin. Biomech. 8 (2015), https://doi.org/10.1016/j.clinbiomech.2014.10.001.
[83] M. Palanca, G. Barbanti-Bròdano, L. Cristofolini, The size of simulated lytic metastases affects the strain distribution on the anterior surface of the vertebra, J. Biomech. Eng. 140 (2018) 111005, https://doi.org/10.1115/1.4040587.
[84] M.J. Silva, J.A. Hipp, D.P. McGowan, T. Takeuchi, W.C. Hayes, Strength reductions of thoracic vertebrae in the presence of transcortical osseous defects: effects of defect location, pedicle disruption, and defect size, Eur. Spine J. 2 (1993) 118–125, https://doi.org/10.1007/BF00301407.
[85] H.-J. Wilke, F. Rohlmann, C. Neidlinger-Wilke, K. Werner, L. Claes, A. Kettler, Validity and interobserver agreement of a new radiographic grading system for intervertebral disc degeneration: part I. Lumbar spine, Eur. Spine J. 15 (2006) 720–730, https://doi.org/10.1007/s00586-005-1029-9.
[86] A. Vernengo, H. Bumann, N. Kluser, A. Soubrier, A. Šećerović, J. Gewiess, J. U. Jansen, C. Neidlinger-Wilke, H.-J. Wilke, S. Grad, Chemonucleolysis combined with dynamic loading for inducing degeneration in bovine caudal intervertebral discs, Front. Bioeng. Biotechnol. 11 (2023) 1178938, https://doi.org/10.3389/fbioe.2023.1178938.
[87] M.A. Adams, P. Pollintine, J.H. Tobias, G.K. Wakley, P. Dolan, Intervertebral disc degeneration can predispose to anterior vertebral fractures in the thoracolumbar spine, J. Bone Mineral Res. 21 (2006) 1409–1416, https://doi.org/10.1359/jbmr.060609.
[88] T.S. Keller, I. Ziv, E. Moejanto, D.M. Spengler, Interdependence of lumbar disc and subdiscal bone properties: a report of the normal and degenerated spine, J. Spinal Disord. 6 (1993) 106–113, https://doi.org/10.1097/00002517-199304000-00003.
[89] P.A. Hulme, S.K. Boyd, S.J. Ferguson, Regional variation in vertebral bone morphology and its contribution to vertebral fracture strength, Bone 41 (2007) 946–957, https://doi.org/10.1016/j.bone.2007.08.019.
[90] P. Pollintine, P. Dolan, J.H. Tobias, M.A. Adams, Intervertebral disc degeneration can lead to “Stress-Shielding” of the anterior vertebral body: a cause of osteoporotic vertebral fracture? Spine (Phila Pa 1976) 29 (2004) 774–782, https://doi.org/10.1097/01.BRS.0000119401.23006.D2.
[91] V.R. Yingling, J.P. Callaghan, S.M. McGill, Dynamic loading affects the mechanical properties and failure site of porcine spines, Clin. Biomech 12 (1997) 301–305, https://doi.org/10.1016/s0268-0033(97)00009-0.
[92] C.M. Whyne, S.S. Hu, J.C. Lotz, Burst fracture in the Metastatically involved spine: development, validation, and parametric analysis of a three-dimensional poroelastic finite-element model, Spine (Phila Pa 1976) 28 (2003) 652–660, https://doi.org/10.1097/01.BRS.0000051910.97211.BA.